Nanoscale

PAPER

Check for updates

Cite this: DOI: 10.1039/d3nr05314h

Nickel as a modifier of calcium oxalate: an *in situ* liquid cell TEM investigation of nucleation and growth†

Lioudmila V. Sorokina,[a] Abhijit H. Phakatkar,[b] Pavel L. Rehak,[c] Petr Král, [ID] [d] Tolou Shokuhfar [ID] [b,e] and Reza Shahbazian-Yassar [ID] *[a,e]

Despite extensive research on the nucleation and growth of calcium oxalate (CaOx) crystals, there are still several challenges and unknowns that remain. In particular, the role of trace metal elements in the promotion or inhibition of CaOx crystals is not well understood. In the present study, *in situ* graphene liquid cell transmission electron microscopy (*in situ* GLC TEM) was used to observe real-time, nanoscale transformations of CaOx crystals in the presence of nickel ions (Ni^{2+}). The results showed that Ni^{2+} form Ni-water complexes, acting as a shape-directing species, generating a unique morphology and altering growth kinetics. Transient adsorption of Ni-water complexes resulted in a metastable phase formation of calcium oxalate trihydrate. Atomistic molecular dynamics simulations confirmed that Ni^{2+} acts as a weak inhibitor which slows down the CaOx crystallization, elucidating that Ni^{2+} impacts small-sized CaOx clusters by bringing more water into the clusters. This work highlighted the intricacies behind the effect of Ni^{2+} on CaOx biomineralization that were made possible to discern using *in situ* GLC TEM.

[a]Department of Civil, Materials, and Environmental Engineering, University of Illinois Chicago, Chicago, IL, 60607, USA. E-mail: rsyassar@uic.edu
[b]Department of Biomedical Engineering, University of Illinois Chicago, Chicago, IL, 60607, USA
[c]Department of Chemistry, University of Illinois Chicago, Chicago, IL, 60607, USA
[d]Departments of Chemistry, Physics, Pharmaceutical Sciences, and Chemical Engineering, University of Illinois Chicago, Chicago, IL, 60607, USA
[e]Department of Mechanical and Industrial Engineering, University of Illinois Chicago, Chicago, IL, 60607, USA
†Electronic supplementary information (ESI) available. See DOI: https://doi.org/10.1039/d3nr05314h

Introduction

Calcium oxalate (CaOx) is an essential biomineral, with a prevalent presence in plant life and geobiological, hydrothermal, and diagenetic processes.[1,2] The role of CaOx as a biomarker led to its potential use in astrobiological investigations.[3,4] However, despite its significance in many aspects of nature, CaOx is implicated in several pathogenic processes, including heart disease, breast cancer, and urolithiasis.[5–7] In case of kidney stones, the presence of CaOx is particularly important as approximately 80% of kidney stones are made up of calcium oxalate.[7] Worldwide, kidney stone disease affects up to 15% of the population, resulting in a significant personal and financial burden.[8] In the U.S. alone, the estimated direct and indirect costs exceeded $5.3 billion in 2000.[9] It is a painful condition that has a recurrence rate of 40% within 5 years after the initial event.[10] Although kidney stone formation has been studied extensively throughout human history, there exist knowledge gaps, particularly in the understanding of the influence of various non-mineral stone constituents on the mineral phase formation.[11]

CaOx forms as a monoclinic calcium oxalate monohydrate (COM, $CaC_2O_4 \cdot H_2O$), tetragonal calcium oxalate dihydrate (COD, $CaC_2O_4 \cdot 2H_2O$), and triclinic calcium oxalate trihydrate (COT, $CaC_2O_4 \cdot 3H_2O$) in its crystalline form.[12] COM is the most thermodynamically stable form and is most frequently found in kidney stones.[13] COD is the metastable form also present in kidney stones: it is capable of transforming into COM.[14] Although not a major constituent of kidney stones and the least thermodynamically stable phase, COT is nevertheless important in that can also give rise to more stable phases.[15] CaOx mineral phases also differ in their adsorptive capabilities when binding various macromolecules that have an outcome on crystal phase and morphological development. In particular, the adsorptive capabilities of COM exceed those of COT, which in turn is greater than that of COD.[12] The mechanisms through which modifiers influence crystal development include the alteration of the morphology *via* binding to preferential faces or by causing lattice distortions, the adjustments in phase stability, and the change in nucleation rates by affecting supersaturation.[16–19] Ionic modifiers, in particular, can impact the solubility and thus, the rate of growth, as well as inhibit growth by interacting directly with crystal surfaces.[20]

For example, cadmium (Cd) underwent sequestering into to the CaOx lattice, causing host lattice distortion in the *c*-direction.[17,18] The addition of magnesium (Mg) induced the formation of COD, a metastable phase of CaOx, as well as impacted the morphology and size of the formed particles, resulting in an inhibitory effect.[18,21–24] In other systems, such as calcite, Mg^{2+} impacted solubility by decreasing effective supersaturation.[25] Another ion found in kidney stones, zinc (Zn), was found to lower nucleation rates by chelating with oxalate and thus, lowering the activity of the latter.[19,26] Presently, there is a limited understanding of the impact ionic modifiers have on the mechanisms of growth of CaOx.

Although the presence of multiple metal ions in kidney stones has been confirmed in patient samples, there is still a dearth of understanding of the mechanisms through which individual ions influence the formation of a stone.[23,26–31] This is particularly relevant for trace elements such as nickel (Ni), which is a reported constituent of kidney stones.[26,31] Previously reported serum and urine concentrations for nickel, an essential trace element, range from 0.1–6.0 µg L^{-1}, with urinary stone composition of nickel ranging from 0.03 to 484 µg g^{-1}.[32–34] Humans obtain Ni through dietary sources as well as through environmental exposure *via* inhalation and dermal contact.[35] Ni presents a double-edge sword in relation to human health. On one hand, it has an effect on iron metabolism and health-promoting gut microbiota while on the other hand, its effects on the immune system as well as carcinogenesis and teratogenicity are well documented.[35–37] However, despite its equivocal nature, Ni has important functions in other organisms. Ni is an essential micronutrient in plants and is a key player in their antioxidant metabolism.[38] Ni also acts as an enzymatic co-factor in the catalysis of bacterial metallo-enzymes.[39] Furthermore, in addition to influencing CaOx crystallization, Ni was also found to impact the mineralization of hydroxyapatite.[40] Ni inhibited the crystallization of the apatitic phase, including the loss of crystal periodicity as well as caused the decrease in thermal stability. In case of brushite, another type of kidney stone constituent, Ni was proposed to serve as a trigger for recurring brushite stone formation, preventing it from converting to hydroxyapatite and further influenced by a decrease in carbonate.[41,42]

There is limited evidence on the effect of Ni on the formation of CaOx – based stones: an *ex situ* study confirmed that Ni acts as a shape-directing species, affecting particle morphology.[43] However, due to the limitations of methods, it was unclear whether Ni ions (Ni^{2+}) affected the nucleation and subsequent growth without incorporation into the crystalline matrix or if the amount of Ni^{2+} was below the limit of detection *via* the energy dispersive X-ray microanalysis. In fact, one of the present challenges in understanding the mechanisms and pathways through which metal ions contribute to the formation of CaOx – based stones stems from the constraints of the experimental methods. For example, differences in distribution of metal ions in the kidney stone composition were observed in various studies.[23,26–31,44] These differences may be attributed to the variability in mineral phase of the analyzed samples, analytical tools, and patient lifestyle factors. Moreover, kidney stone mineralization *in vivo* is influenced by numerous environmental factors, such as localized pH, ionic concentration, and the presence of biomolecules, thus making it challenging to isolate the effect of a particular ion on biomineralization. Together with lack of *in situ* models that observe stone formation in real time, there exists a need to discern the mechanisms in which ions, such as Ni^{2+}, impact mineral phase development.

To narrow the knowledge gap in our understanding of Ni^{2+}'s impact on CaOx crystallization, we utilized *in situ* graphene liquid cell (GLC) transmission electron microscopy (TEM). The use of GLC allows for observation of the nucleation and growth events of biological crystals *in situ*, in real time, and on the nanoscale while maintaining high spatial resolution, protecting the sample from the column pressure and minimizing the radiation damage.[45,46] Prior work using *in situ* GLC TEM revealed that the addition of citrate, a known inhibitor, to CaOx results in the increased hydration state of the crystal *via* the formation of calcium-citrate complexes which, in turn, prevents oxalate binding.[47] In the present study, we elucidated the effect of Ni^{2+} on CaOx crystallization *in situ* and at atomic level resolution, and observed its impact on phase stability and particle morphology – important differentiators in nanocrystals of lithogenic and healthy patients.[48] It was determined that through the formation of Ni-water complexes, Ni^{2+} has a dual surface effect as both a crystal stabilizer as well as directional growth inhibitor, impacting the crystal morphology. Moreover, as Ni-water complexes interact with the surface of CaOx, this leads to the amorphization and a metastable phase formation. Atomistic molecular dynamics (MD) simulations confirmed the role of Ni^{2+} as a weak inhibitor and its effect on the growth rate *via* the introduction of additional water to the surface of CaOx.

Experimental

Preparation of graphene-coated TEM grids

Graphene-coated TEM grids were prepared following a previously confirmed protocol.[46] Briefly, a desired area of a CVD-deposited monolayer of a graphene-on-copper foil (Grolltex) was obtained and its wrinkles were removed using two glass slides (Fisherbrand) and a nonwoven wipe (Texwipe). The amorphous carbon sides of Quantifoil R2/2 micromachined holey carbon grids, 200 mesh gold (SPI Supplies), were placed in contact with graphene and bonded for at least two hours *via* the addition of isopropyl alcohol. Copper was subsequently etched by placing the grids, together with the graphene-on-copper, in a solution of 1 g of sodium persulfate (MilliporeSigma) in 10 mL deionized water for 12 hours. Copper etching was followed by rinsing the grids 3 times in HPLC-grade water (MilliporeSigma) and air drying.

Sample preparation

Control calcium oxalate (CaOx) sample was prepared by combining equimolar $CaCl_2$ (Fischer Chemical) and $Na_2C_2O_4$

(Sigma-Aldrich). The product formed instantaneously in the following reaction: $Na_2C_2O_4 + CaCl_2 \rightarrow CaC_2O_4 + 2NaCl$. A sample containing Ni was prepared by combining 0.03 M $CaCl_2$ and $Na_2C_2O_4$ with 0.004 M $NiCl_2$. The solutions were prepared immediately prior to encapsulation. 0.3 μL of reaction solution was encapsulated between two graphene-coated TEM grids.

Characterization

All characterization was performed using JEOL JEM-ARM200CF aberration-corrected scanning transmission electron microscope. To assess nanoparticle morphology, the microscope was operated in STEM mode at 200 kV and with a 22 mrad convergence angle. High-angle annular dark field (HAADF) imaging was performed using an Orius CCD camera with a 512 × 512 scanning resolution. Quantitative chemical analysis was done *via* STEM-EDS at 200 kV utilizing the Oxford EDS detector system, with a pixel dwell time of 500 μs. Selected area electron diffraction (SAED) analysis was performed in a TEM diffraction mode with the camera length of 25 cm. High resolution transmission electron microscopy (HR-TEM) imaging was achieved at 200 kV in TEM mode. The electron dose rate was maintained at 0.015 electrons/Å^2/s. Orius CCD camera with a capture rate of 6 frames per second was used for the acquisition of *in situ* TEM videos.

MD simulations

MD simulations were performed with NAMD3.[49] Water molecules were described using TIP3P model.[50] Monoatomic ions were modelled using Lennard-Jones parameters and integral charges.[51,52] Parameters of oxalate ions were determined from our previous study.[47] The simulations were performed in the NPT ensemble at temperature of 310 K and pressure of 1 atm using a Langevin dynamics with $\gamma_{Lang} = 1.00$ ps^{-1}. The particle-mesh Ewald (PME) method[53] was used together with periodic boundary conditions for evaluation of long-range Coulomb interactions, where the long-range interactions were evaluated every 1 (van der Waals) and 2 (coulombic) time steps. The systems were minimized for 5000 steps and pre-equilibrated for 2000 steps, with a time step set to 2.0 fs. All simulations had the same number of waters, calcium ions, and oxalate ions, such that [CaOx] = 30 mM. There was a total of 145 oxalate ions in all simulations; spectator NaCl ions were also added into the system to replicate experimental conditions. One carbon atom on each oxalate molecule was harmonically constrained to allow these molecules to rotate, but not diffuse during minimization and pre-equilibration. There were no constraints during the simulations, which ran for over 400 ns with a time step of 2.0 fs.

In the analysis, a cluster was defined by having at least one Ca^{2+} ion and one oxalate, where they were in at least 4.5 Å of each other. Cluster sizes were iteratively determined by analyzing a central cluster of oxalate, nickel ions, or calcium ions and determining whether they were different molecules of those same species (neighbors) within 4.5 Å of the first central cluster. Iterations ended when no new neighbors were found.

After the cluster size was determined, the number of water molecules that were within 4.5 Å of any calcium ion, oxalate molecule, or nickel ion in the final cluster were determined. To eliminate artifacts of having a finite simulation box, it was determined whether any molecule in the final cluster was within 4.5 Å of the boundary of simulation box. If there was a cluster close to the boundary of the box, the entire cluster and neighboring water molecules were displaced by the dimension of the corresponding boundary, yet opposite in direction. We then repeated the iterations as described earlier. Sizes of clusters were determined by the number of calcium ions in that cluster. Evaluations of cluster sizes were determined for every 1.00 ns, due to memory limitations.

Results and discussion

The observation of *in situ* nanoscale CaOx crystallization in real time was performed using GLC TEM. An aqueous solution containing ions of interest was encapsulated between two graphene-coated TEM grids, forming a liquid cell *via* van der Waals interactions between graphene sheets. The schematic representation of a GLC is shown in Fig. 1a. The control sample GLC contained a solution with calcium and oxalate ions, illustrated using a blue box. Another GLC encapsulated a solution with calcium, oxalate, and nickel ions is highlighted by the pink box. The precipitation reaction leading to the formation of CaOx is instantaneous and is not due to the electron beam given the constant electron dose rate, as previously demonstrated.[47,54] Fig. S1† shows the results of the beam-blank experiment, where after 300 s of beam-blanking a COT nanoparticle maintains its phase and size. This further confirms that this is not a beam-driven reaction and that the beam did not induce radiation damage. Fig. 1b shows the *in situ* GLC high-angle annular dark-field scanning transmission electron microscopy (HAADF-STEM) image of formed CaOx nanoparticles (NPs). In HAADF-STEM, heavier elements appear brighter due to the stronger signal sensed by HAADF detector from a higher number of inelastically scattered primary electrons. Thus, in Fig. 1b, the brightest spots correspond to areas of high calcium concentration, suggesting a non-specific distribution throughout the NPs. The NPs are characterized by a distinctive morphology of sharp edges and tips. Fig. S2a† provides TEM micrographs of the control CaOx NPs whereas Fig. S2b† shows TEM micrographs of CaOx-Ni NPs, confirming morphologies observed in STEM. This morphology was also observed in nanocrystals formed in the urine of lithogenic patients and is associated with improved crystal attachment and injury to renal epithelial cells.[48] Moreover, NPs of similar size show some agglomeration, a feature also associated with the pathology.

By contrast, CaOx NPs formed with the presence of Ni^{2+} ions in the solution do not have distinguishable crystalline features, as illustrated by Fig. 1c and S2b,† suggesting their limited ability to inflict cellular damage. Perhaps the most important finding is that the addition of Ni^{2+} alters the crystal
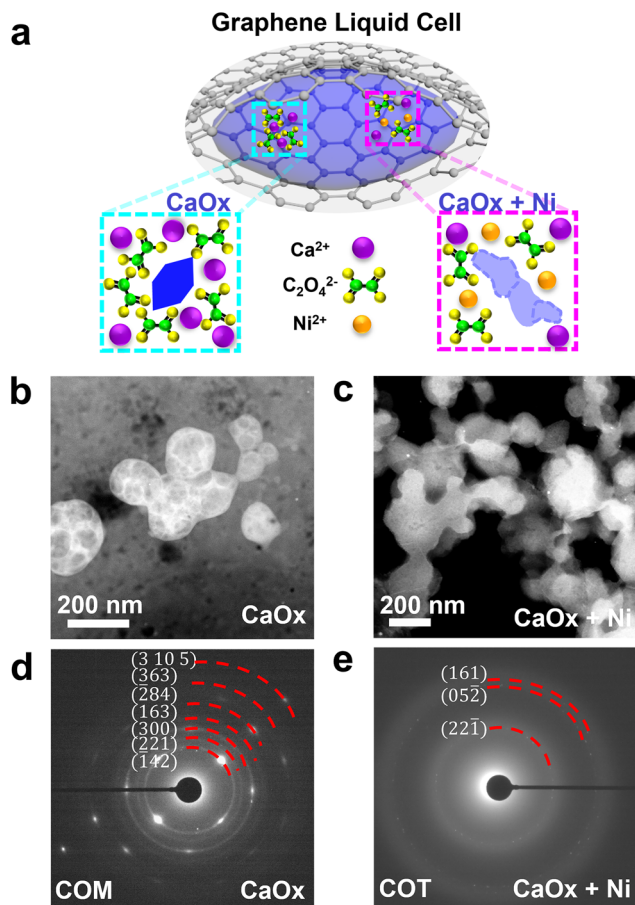
Fig. 1 (a) A graphical representation of a GLC containing an aqueous solution with ions of interest. Two layers of graphene encapsulate a droplet of an aqueous solution. A solution containing calcium and oxalate ions is highlighted by the blue box. A pink box highlights a solution that includes calcium, oxalate, and nickel ions. (b) *In situ* GLC HAADF-STEM image of calcium oxalate. (c) *In situ* GLC HAADF-STEM image of calcium oxalate with nickel. (d) *In situ* GLC SAED of calcium oxalate monohydrate (COM) formed in the absence of nickel. (e) *In situ* GLC SAED of calcium oxalate trihydrate (COT) formed in the presence of nickel.

phase, resulting in a less thermodynamically stable structure. Fig. 1d illustrates the results of *in situ* GLC selected area electron diffraction (SAED) of COM formed in the absence of Ni^{2+}, obtained for structural confirmation from a large region of NPs. The data shows the presence of multiple crystal planes such as $(\bar{1}42)$, (221), (300), (163), $(\bar{2}84)$, (363), (3105), characterized by well-defined bright spots.[55] By contrast, in the presence of Ni^{2+}, the existence of COT is observed, as indicated by $(22\bar{1})$, $(05\bar{2})$, (161).[56] Moreover, diffused and broader rings in Fig. 1e suggest that many of the NPs formed were amorphous in nature, with some metastable COT present.

This finding is a key confirmation of the effect of Ni^{2+} on CaOx formation, suggesting that Ni^{2+} favorably alters the crystal phase. Specifically, the crystal phase is the most important factor in crystal adhesion and subsequent cell injury at the nanoscale since it is possible to eliminate larger size crystals as long as they do not attach. The adhesion of COM crys-

tals to renal epithelial cells is stronger than those of a metastable phase.[57] Thus, by acting as a phase modifier, Ni has the potential to reduce the chance of crystal to cell adhesion.

In situ GLC energy-dispersive X-ray spectroscopy (EDS) was used to better understand the mechanism through which Ni^{2+} ions affect CaOx crystallization. Fig. 2 illustrates *in situ* STEM-EDS elemental analysis of CaOx control NPs as well as those doped with Ni^{2+} as they formed in an aqueous environment. Fig. 2a shows an *in situ* GLC STEM-HAADF image overlaid with Ca and O elemental mapping. Details of elemental distribution are elaborated on in Fig. 2b. Specifically, the distribution of Ca is homogenous and is concentrated primarily in the CaOx NPs. A trace amount of Ca is observed in the areas close to the NP, which is in line with the expectation that some Ca ions are floating in the solution. Distribution of O follows the distribution of Ca, with additional O present outside of the NPs. This is also expected since the NPs are formed in water.

Fig. 2c shows an *in situ* GLC STEM-HAADF image overlaid with Ca, O, and Ni elemental mapping. The elemental distribution of Ca and O in a Ni-doped sample in Fig. 2d is similar to the control CaOx sample in Fig. 2b. Fig. 2d clearly demonstrates that Ni^{2+} ions are present in the CaOx NPs. Ni is uniformly distributed within the NPs, appearing at both the edges as well as the center of the structures. Fig. S3† provides deconvoluted spectra for both the control and CaOx + Ni conditions.
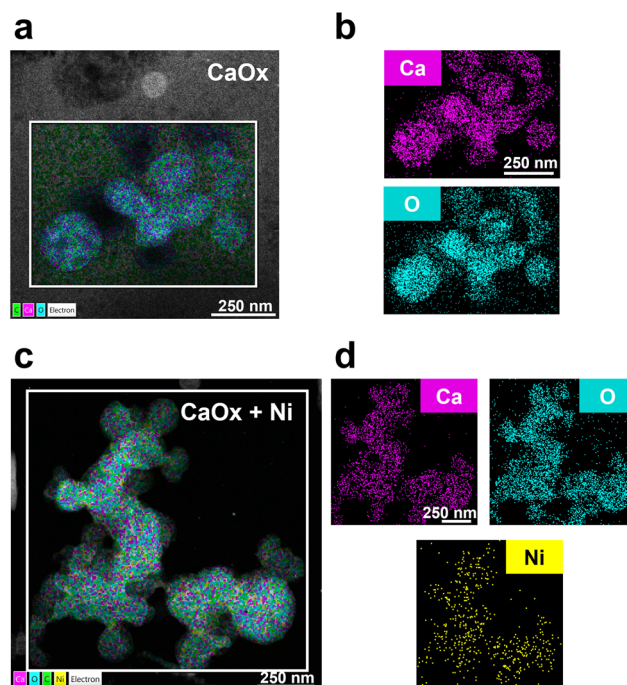

Fig. 2 *In situ* STEM-EDS elemental analysis of CaOx in the absence and presence of Ni in GLC aqueous environment. (a) *In situ* GLC STEM-HAADF overlay with elemental mapping of CaOx NPs. (b) Individual *in situ* GLC STEM-EDS elemental mapping of Ca and O in CaOx NPs. (c) *In situ* GLC STEM-HAADF overlay with elemental mapping of CaOx in the presence of Ni. (d) Individual *in situ* GLC STEM-EDS elemental mapping of Ca, O, and Ni, confirming the interaction of Ni with the CaOx structure.

The atomic% ratio of O to Ca ($\sim$4 : 1) reported in Fig. S3a† is consistent with our expectations for the ratios found in calcium oxalate based on the formula CaC_2O_4. The atomic% of Ni is reported in Fig. S3b† at 2.3%, which is in line with doping concentration expectations. Moreover, Ni-Lα and Ni-Kα peaks were observed at 0.851 and at 7.471, respectively, confirming the presence of Ni in the sample. EDS has been used in the past to verify the formation of CaOx as well as to analyze the inclusions of heavy metals in the CaOx structure in the *ex situ* samples.[17,43,47,58] To date, using EDS to verify the incorporation of metal ions in CaOx matrix *ex situ* resulted in inconclusive data regarding the possibility of Ni element's interaction with the CaOx matrix, potentially due to experimental limitations.[43] This work clearly demonstrates the advantage of using *in situ* GLC STEM-EDS to identify the interaction of Ni^{2+} ions with the CaOx structure at a doping concentration during real-time NP formation.

Fig. 3 illustrates the growth of a single CaOx NP doped with Ni^{2+} ions *in situ*. The nucleus forms at 0.2 seconds, showing crystalline growth of $(10\bar{1})$ and (212) COT planes and measuring 8.2 nm^2 (Video S1, Fig. S4 and S5†).[56] The $(10\bar{1})$ remains present through all the time points, with an addition of new planes with time. The growth phase occurs in two stages: from 0.2 seconds to 9.0 seconds at the rate of 8.04 nm^2 s^{-1} and from 9.0 to 26.8 seconds at the rate of 1.38 nm^2 s^{-1} (Fig. S5†). In the first stage, the ions from the bulk solution are diffused to the crystal surface.[59,60] Here, the presence of Ni^{2+} ions on the crystal surface is likely to be negligible since the crystal continues to grow at a high rate. In the second stage, the attachment and subsequent incorporation of the ions into the crystal lattice occurs *via* a first-order reaction. The overall process of crystallization may be represented by the following equation:

$$\frac{dm}{dt} = K_G A (c - c^*)^g \tag{1}$$

where m refers to the mass of deposited solid, t represents time, K_G stands for the overall crystal growth coefficient, A is the surface area of the crystal, c is the supersaturated solute concentration in the solution, c^* is the equilibrium saturation concentration, and g refers to the overall crystal growth exponent.[61]

A drastic decrease in the growth rate may also be attributed to the increased presence of Ni^{2+} ions on the crystal surface which inhibits the attachment of calcium and oxalate ions. Thus, Ni^{2+} ions act as defects and prevent further growth along a particular crystallographic face, ultimately resulting in agglomerations observed in Fig. 1c. Moreover, by 26.8 seconds, the crystal is likely approaching a critical defect concentration, thereby further slowing the growth.

The impact of Ni^{2+} as a defect may be further understood by examining its effect on Gibbs free energy given by the following equation:

$$G = G^* + N_D \Delta H_D - T N_D \Delta S_v - T \Delta S_c(N_D) \tag{2}$$

where G represents Gibbs free energy, G^* is the Gibbs free energy of a perfect crystal, N_D represents the number of defects, ΔH_D is the change in enthalpy per defect, T is temperature, ΔS_v refers to the change in vibrational entropy per defect, and $\Delta S_c(N_D)$ represents the change in configurational entropy as a function of the number of defects.[62] Since the crystal maintains the same phase throughout the transformations (COT), the impact of the change in configurational entropy is negligible. As a crystal grows, the number of defects increases. This suggests that at a larger crystal size, the increased number of defects will cause the enthalpy and entropy to come to a point at which it is no longer favourable for the crystal to grow.

To further elucidate the effect of effect Ni^{2+} ions on the CaOx crystallization, atomistic molecular dynamics (MD) simulations of Ca^{2+} and $C_2O_4^{2-}$ aqueous solutions of [CaOx] =
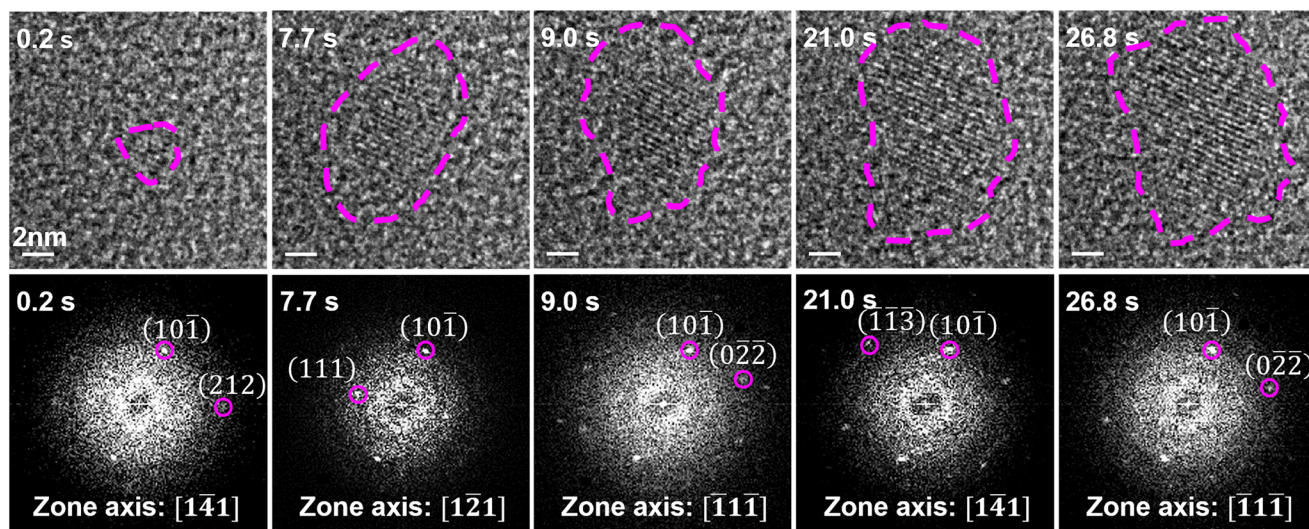

Fig. 3 *In situ* GLC HRTEM time-lapse nucleation and growth of a COT crystal in the presence of Ni^{2+} and corresponding fast Fourier transformations (FFTs).

30 mM were performed in the presence of Ni^{2+} ions at 0, 2, 4, and 8 mM concentrations (see Experimental). In all simulations, the CaOx clusters form and gradually grow. However, Ni^{2+} ions tend to transiently (10–50 ps) adsorb on these CaOx clusters (Fig. 4a (insert)) and slow down their growth. Therefore, Ni^{2+} ions act as a weak inhibitor which slows down the CaOx crystallization, unlike citrate ions which tend to limit the size of CaOx clusters.[47]

Fig. 4shows the results of 4 mM Ni^{2+} simulations, while the other systems are shown in ESI (Fig. S6 and S7†). Fig. 4a provides the ratio of water (within 4.5 Å within CaOx cluster) and Ca^{2+} ions as a function of the number of Ca^{2+} ions present in the clusters. In small clusters, there is a higher water : Ca^{2+} ratio (30–80) with a large variability regardless of the Ni^{2+} concentration in the solution. When more than 15–20 Ca^{2+} ions are in the cluster, the water : Ca^{2+} ratio converges to ~10 water molecules. It turns out that the presence Ni^{2+} ions in the solution doesn't affect much this limiting ratio.

These results can be better understood from Fig. 4b, which reveals that larger Ni^{2+} : Ca^{2+} ratio are limited to smaller cluster, since the Ni^{2+} ions are practically only adsorbed at the CaOx cluster surfaces. Moreover, these smaller clusters have a higher water : Ca^{2+} ratios (30–60), which shows that when Ni^{2+} interacts with the CaOx cluster it brings more water into the cluster. These data support the experimental observation showing that integration of Ni^{2+} in the CaOx crystal is accompanied with more water but also with a loss of crystallinity since the Ni is not well integrated within the CaOx system, as revealed by these simulations.

The proposed mechanism of the effect of Ni^{2+} on CaOx crystal growth is outlined in Fig. 5 and described in detail as follows. Calcium and oxalate ions encapsulated in GLC in a supersaturated aqueous environment undergo an instantaneous precipitation reaction, leading to the nucleation of a COT crystal.[46,47,54] Ni^{2+}, present in a solution at a doping concentration, form Ni-water complexes *via* interactions with water. This presents an opportunity for Ni-water complexes to interact with the surface of the COT crystal, for example, with water that is part of the crystal structure and is located on the

surface. This interaction produces a dual effect. First, a Ni-water complex brings additional water molecules, thereby increasing the hydration state of the structure. Second, a Ni-water complex influences the direction of growth by interacting with the water on the crystal surface and thus preventing new growth of CaOx at those particular sites. As additional calcium and oxalate ions are incorporated into the lattice structure, a Ni-water complex becomes incorporated in the growing structure. Since the newly incorporated ions must grow around Ni-water complexes on the surface, the resulting shape of the crystal becomes distorted, as shown in Fig. 1c.

The addition of excess water into the crystal structure prevents the rearrangement of COT into a more stable phase over time. The presence of Ni-water complexes may also induce local strain resulting in an amorphous morphology with some metastable COT present.[25,55] Prior experimental and computational findings established that the presence of a CaOx molecular inhibitor produces a localized lattice strain, resulting in the release of calcium and oxalate ions to alleviate the strain.[63] Moreover, the lattice strain increases crystal solubility while decreasing the solubility of the solution, thus impacting the thermodynamic equilibrium.[25]

Hydrated Ni(II) has been extensively investigated as it is found as a constituent of many single crystals with a variety of applications.[64–66] Hydrated Ni(II) ion consists of six water molecules in its first coordination sphere in an octahedral arrangement, with the O–N–O angle variability of up to 20 degrees.[64] The second hydration sphere ranges between 13 and 16 water molecules, depending on the computational approach.[64,65] 13 water molecules in the second hydration sphere are considered to have a nearly ideal arrangement *via* hydrogen bonding whereas in a 16-water scenario, the additional water molecules are included without any specific arrangement in addition to those occurring *via* hydrogen bonds. Overall, this demonstrates that the inclusion of hydrated Ni(II) brings about additional water, as reflected in the increased hydration state of the structure. In addition, the water exchange reaction between a water in hydrated Ni(II) and an outside water molecule occurs *via* a dissociative mode of activation. Furthermore, water exchange occurs in the first coordination sphere due to the initial structural distortion. Since the increase in the ionic radius decreases the binding energies, a water molecule is more likely to bind to nickel than to calcium.[67,68] This provides an opportunity for a water exchange to occur between a water molecule from hydrated Ni(II) and a water on the surface of the COT crystal, ultimately resulting in the interaction with the hydrated Ni(II) and the formation of the most hydrated crystal form of CaOx with some amorphization, as observed here experimentally.

While these findings pave the way for high throughput nanoscale investigations of metal modifiers on calcium oxalate, it is important to acknowledge the limitations of the present methodology. Specifically, current study is a simplified system that focuses on observing an isolated effect of Ni during CaOx biomineralization without considering additional biological and chemical factors that take place in an *in vivo*
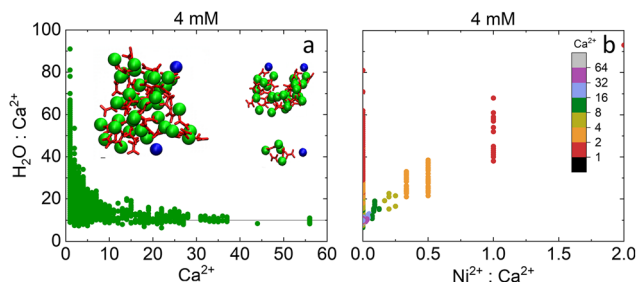

Fig. 4 (a) Number of water molecules within 4.5 Å per Ca^{2+} ion in a cluster *vs.* number of Ca^{2+} ion within a cluster. (Inset) Three clusters at *t* = 300 ns. Green atoms represent Ca^{2+} ion; blue atoms represent Ni^{2+} ions, red atoms are $C_2O_4^{2-}$ ions. Scale bar is 1 Å. (b) Number of water molecules within 4.5 Å per Ca^{2+} ion in a cluster *vs.* ratio of Ni^{2+} ions within 4.5 Å of a cluster with respect to number of Ca^{2+} ions in a cluster. Color scale shows the number of Ca^{2+} in cluster.

COT nucleus formation

COT crystal partial growth and Ni-water complexes formation

COT interaction with Ni-water complexes

$\bullet Ca^{2+}$ $\bullet O^{2-}$ $\bullet H_2O$ $\bullet Ni^{2+}$

COT amorphization with incorporated Ni-water complexes

Ni-water complexes incorporation

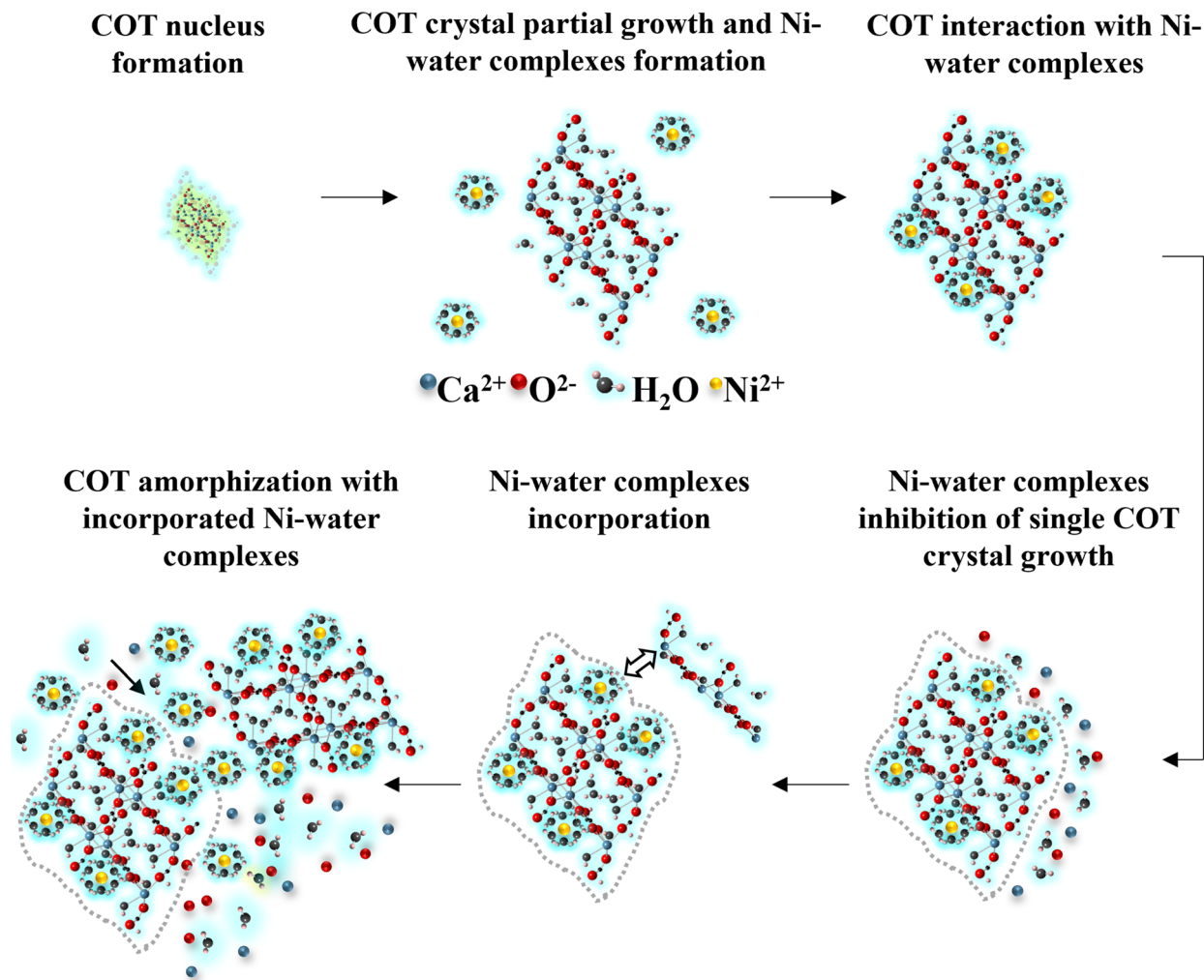**Ni-water complexes inhibition of single COT crystal growth**

Fig. 5 Proposed mechanism of the effect of Ni on CaOx crystal growth. CaOx nucleates as COT and undergoes partial growth. Ni ions forms a Ni-water complex through interactions with water. A Ni-water complex is incorporated on the periphery of the crystal, introducing additional water. As the structure grows, the incorporation of Ni-water complexes results in a distorted shape and the inability to transform into a more stable phase.

system. Crystallization occurs at higher than physiological concentrations to account for the limited field-of-view, to avoid prolonged beam exposure, and to stay within EDS detection limits. Additional limitation of the *in situ* GLC TEM approach is the inability to modify or to measure the temperature within the GLC nanoreactor during the duration of the experiment. To study CaOx crystallization at a constant, physiologically – relevant temperature in the future, additional liquid cell approaches such as the use of a heated liquid cell holder may be considered. Despite these shortcomings, present results are consistent with the previous limited knowledge about the impact of Ni^{2+} on CaOx crystallization.[43] Current study confirmed that Ni^{2+} acts as a shape-directing species, resulting in phase change. However, a distinguishing aspect of this work is the elucidation of the mechanism through which Ni^{2+} impacts the crystallization of CaOx. It was determined that Ni^{2+} has a dual surface effect that leads to crystal stabilization and growth inhibition in the specific directions where Ni^{2+} is present, as evident by a distinct morphology. Ni^{2+} does not

diffuse into the crystal lattice but rather, becomes incorporated by forming Ni-water complexes and interacting with the water in the hydrated CaOx crystal, thus leading to amorphization. The finding of the most clinical significance is that the addition of Ni^{2+} leads to a more hydrated crystal phase, metastable COT, as compared to control, COM. CaOx crystal phase is the most important factor on the outcomes of crystal attachment and cell injury *in vitro*. Thus, by increasing the hydration state, Ni^{2+} prevents the formation of a more stable, detrimental phase. The importance of the methodologies employed in this study should also be noted. For example, it was possible to establish the localized interaction of Ni^{2+} with the CaOx structure due to the use of *in situ* GLC STEM-EDS. The kinetic effect of Ni was determined in real time and at atomic resolution by using *in situ* GLC HR-TEM. This highlights the effectiveness of the use of *in situ* GLC TEM and opens possibilities for the future real-time nanoscale investigations on the effects of metal ions on CaOx crystallization. Overall, this study demonstrated the complexity and equivocalness of Ni^{2+} on the formation of CaOx and

the need for effective *in situ* methodologies to evaluate metal ions effects on CaOx on the nanoscale.

Conclusions

Present study elucidated the effect of Ni^{2+} on CaOx crystallization, specifically on crystal phase, morphology, and growth kinetics. The findings established that Ni^{2+} acts as a shape-directing species, resulting in particles that do not have a distinguishable crystalline morphology. Moreover, in the presence of Ni^{2+}, the least thermodynamically crystalline phase, COT, was observed. By interacting with the surface of the nanocrystal, Ni^{2+} impacted the growth rate.

Atomistic MD simulations further clarified the inhibitory mechanism by showing that Ni^{2+} ions are transiently adsorbed on small-sized CaOx clusters, thereby affecting the rate of crystallization. Future MD simulations efforts should evaluate additional parameters, such as the effect of Ni^{2+} on the supersaturation of CaOx and the subsequent impact on nucleation and growth. Moreover, due to the experimental limitations of the system, additional computational efforts to test the impedance of Ni^{2+} on COM growth and to further discern the pathway of COT formation at different concentrations may be considered. Presently, the incorporation of Ni^{2+} into the CaOx crystal results in additional water and a loss of crystallinity since the Ni^{2+} is not well integrated within the CaOx system. The presented results are of significance to pathological CaOx mineralization as they illustrate the inhibitory potential of Ni^{2+}.

Author contributions

Lioudmila V. Sorokina: conceptualization, formal analysis, investigation, methodology, visualization, writing – original draft. Abhijit H. Phakatkar: investigation, methodology, formal analysis, writing – review & editing. Pavel L. Rehak: investigation, methodology, formal analysis, writing – original draft. Petr Král: conceptualization, writing – review & editing. Tolou Shokuhfar: funding acquisition, conceptualization. Reza Shahbazian-Yassar: supervision, funding acquisition, conceptualization, writing – review & editing.

Conflicts of interest

There are no conflicts of interest to declare.

Acknowledgements

References

1 V. Franceschi, *Trends Plant Sci.*, 2001, **6**, 331.
2 B. A. Hofmann and S. M. Bernasconi, *Chem. Geol.*, 1998, **149**, 127–146.
3 Z. Cheng, D. Fernández-Remolar, M. Izawa, D. Applin, M. Chong Díaz, M. Fernandez-Sampedro, M. García-Villadangos, T. Huang, L. Xiao and V. Parro, *J. Geophys. Res.: Biogeosci.*, 2016, **121**, 1593–1604.
4 J.-J. Zhao, Y.-F. Zhang, T.-L. Zhao, H. Li, Q.-Z. Yao, S.-Q. Fu and G.-T. Zhou, *Astrobiology*, 2022, **22**, 35–48.
5 Z. Bahadoran, P. Mirmiran and F. Azizi, *Nutr. J.*, 2022, **21**, 1–8.
6 A. M. Castellaro, A. Tonda, H. H. Cejas, H. Ferreyra, B. L. Caputto, O. A. Pucci and G. A. Gil, *BMC Cancer*, 2015, **15**, 1–13.
7 S. R. Khan, M. S. Pearle, W. G. Robertson, G. Gambaro, B. K. Canales, S. Doizi, O. Traxer and H.-G. Tiselius, *Nat. Rev. Dis. Primers*, 2016, **2**, 1–23.
8 V. Romero, H. Akpinar and D. G. Assimos, *Rev. Urol.*, 2010, **12**, e86.
9 C. S. Saigal, G. Joyce, A. R. Timilsina and U. D. i. A. Project, *Kidney Int.*, 2005, **68**, 1808–1814.
10 E. M. Worcester and F. L. Coe, *N. Engl. J. Med.*, 2010, **363**, 954–963.
11 A. Tefekli and F. Cezayirli, *Sci. World J.*, 2013, **2013**, 1–5.
12 V. Thongboonkerd, T. Semangoen and S. Chutipongtanate, *Clin. Chim. Acta*, 2006, **367**, 120–131.
13 A. R. Izatulina, V. V. Gurzhiy, M. G. Krzhizhanovskaya, M. A. Kuz'mina, M. Leoni and O. V. Frank-Kamenetskaya, *Cryst. Growth Des.*, 2018, **18**, 5465–5478.
14 B. Tomžič and G. Nancollas, *J. Urol.*, 1982, **128**, 205–208.
15 S. Deganello, *Scanning Electron Microsc.*, 1986, **1986**, 45.
16 J. D. Rimer, Z. An, Z. Zhu, M. H. Lee, D. S. Goldfarb, J. A. Wesson and M. D. Ward, *Science*, 2010, **330**, 337–341.
17 E. Weber, D. Levy, M. B. Sasson, A. N. Fitch and B. Pokroy, *RSC Adv.*, 2015, **5**, 98626–98633.
18 M. B. McBride, M. Frenchmeyer, S. E. Kelch and L. Aristilde, *J. Colloid Interface Sci.*, 2017, **486**, 309–315.
19 T. Barker, M. Boon and F. Jones, *J. Cryst. Growth*, 2020, **546**, 125777.
20 K. N. Olafson, R. Li, B. G. Alamani and J. D. Rimer, *Chem. Mater.*, 2016, **28**, 8453–8465.
21 X. Yang, *Indian J. Chem., Sect. A: Inorg., Bio-Inorg., Phys., Theor. Anal. Chem.*, 2020, **57**, 9–17.
22 F. Grases, C. Genestar and A. Millan, *J. Cryst. Growth*, 1989, **94**, 507–512.
23 I. H. Atakan, M. Kaplan, G. Seren, T. Aktoz, H. Gül and O. Inci, *Int. Urol. Nephrol.*, 2007, **39**, 351–356.
24 W. Berg, A. Hesse and H.-J. Schneider, *Urol. Res.*, 1976, **4**, 161–167.
25 K. J. Davis, P. M. Dove and J. J. De Yoreo, *Science*, 2000, **290**, 1134–1137.
26 A. A. Shaltout, M. M. Dabi, S. I. Ahmed, A. S. Al-Ghamdi, E. Elnagar and R. Seoudi, *Biol. Trace Elem. Res.*, 2021, **199**, 2858–2868.

27 S. Galassini, N. Liu, G. Moschini, A. Tasca, G. Villi and V. Valkovic, *Nucl. Instrum. Methods Phys. Res., Sect. B*, 1989, **43**, 556–559.

28 C. Pineda-Vargas, A. Rodgers and M. Eisa, *Radiat. Phys. Chem.*, 2004, **71**, 947–950.

29 D. Bazin, P. Chevallier, G. Matzen, P. Jungers and M. Daudon, *Urol. Res.*, 2007, **35**, 179–184.

30 B. Keshavarzi, N. Yavarashayeri, D. Irani, F. Moore, A. Zarasvandi and M. Salari, *Environ. Geochem. Health*, 2015, **37**, 377–389.

31 Y. Yen, B. Cheng, C. Chan, C. Lin and H. Chen, *Biol. Trace Elem. Res.*, 2018, **185**, 266–274.

32 D. M. Templeton, F. W. Sunderman Jr. and R. F. Herber, *Sci. Total Environ.*, 1994, **148**, 243–251.

33 P. Heitland and H. D. Köster, *Clin. Chim. Acta*, 2006, **365**, 310–318.

34 A. Dargahi, S. Rahimpouran, H. M. Rad, E. Eghlimi, H. Zandian, A. Hosseinkhani, M. Vosoughi, F. Valizadeh and R. Hossinzadeh, *J. Trace Elem. Med. Biol.*, 2023, **80**, 127270.

35 B. Zambelli and S. Ciurli, *Interrelations between essential metal ions and human diseases*, 2013, pp. 321–357.

36 F. H. Nielsen, T. R. Shuler, T. G. McLeod and T. J. Zimmerman, *J. Nutr.*, 1984, **114**, 1280–1288.

37 C. C. Lu, N. Matsumoto and S. Iijima, *Teratology*, 1979, **19**, 137–142.

38 C. C. Fabiano, T. Tezotto, J. L. Favarin, J. C. Polacco and P. Mazzafera, *Front. Plant Sci.*, 2015, **6**, 754.

39 A. Vannini, E. Pinatel, P. E. Costantini, S. Pelliciari, D. Roncarati, S. Puccio, G. De Bellis, C. Peano and A. Danielli, *Sci. Rep.*, 2017, **7**, 1–14.

40 J. Guerra-López, R. Pomés, C. D. Védova, R. Vina and G. Punte, *J. Raman Spectrosc.*, 2001, **32**, 255–261.

41 J. R. Guerra-López, J. A. Güida, M. A. Ramos and G. Punte, *J. Mol. Struct.*, 2017, **1137**, 720–724.

42 J. R. Guerra-López, J. Güida, A. E. Bianchi and G. Punte, *J. Solid State Chem.*, 2018, **267**, 98–105.

43 K. Akhtar and I. U. Haq, *Clin. Chim. Acta*, 2013, **418**, 12–16.

44 K. Ramaswamy, D. W. Killilea, P. Kapahi, A. J. Kahn, T. Chi and M. L. Stoller, *Nat. Rev. Urol.*, 2015, **12**, 543–557.

45 K. He, T. Shokuhfar and R. Shahbazian-Yassar, *J. Phys.: Condens. Matter*, 2019, **31**, 103001.

46 J. Zhang, L. Lin, L. Sun, Y. Huang, A. L. Koh, W. Dang, J. Yin, M. Wang, C. Tan and T. Li, *Adv. Mater.*, 2017, **29**, 1700639.

47 D. J. Banner, E. Firlar, P. Rehak, A. H. Phakatkar, T. Foroozan, J. K. Osborn, L. V. Sorokina, S. Narayanan, T. Tahseen and Y. Baggia, *Adv. Funct. Mater.*, 2021, **31**, 2007736.

48 J.-Y. He, S.-P. Deng and J.-M. Ouyang, *IEEE Trans. NanoBiosci.*, 2010, **9**, 156–163.

49 J. C. Phillips, R. Braun, W. Wang, J. Gumbart, E. Tajkhorshid, E. Villa, C. Chipot, R. D. Skeel, L. Kale and K. Schulten, *J. Comput. Chem.*, 2005, **26**, 1781–1802.

50 W. L. Jorgensen, J. Chandrasekhar, J. D. Madura, R. W. Impey and M. L. Klein, *J. Chem. Phys.*, 1983, **79**, 926–935.

51 D. Beglov and B. Roux, *J. Chem. Phys.*, 1994, **100**, 9050–9063.

52 Y. Won, *J. Phys. Chem. A*, 2012, **116**, 11763–11767.

53 T. Darden, D. York and L. Pedersen, *J. Chem. Phys.*, 1993, **98**, 10089–10092.

54 K. Rewatkar, D. Shende and K. Wasewar, *Chem. Biochem. Eng. Q.*, 2018, **32**, 11–18.

55 V. Tazzoli and C. Domeneghetti, *Am. Mineral.*, 1980, **65**, 327–334.

56 R. Basso, G. Lucchetti, L. Zefiro and A. Palenzona, *Neues Jahrb. Mineral.*, 1997, **2**, 84–96.

57 X. Sheng, M. D. Ward and J. A. Wesson, *J. Am. Soc. Nephrol.*, 2005, **16**, 1904–1908.

58 D. Jáuregui-Zúñiga, M. A. Ferrer, A. A. Calderón, R. Muñoz and A. Moreno, *J. Plant Physiol.*, 2005, **162**, 1183–1187.

59 A. Berthoud, *J. Chim. Phys.*, 1912, **10**, 624–635.

60 J. Valeton, *Z. Kristallogr. – Cryst. Mater.*, 1924, **60**, 1–38.

61 J. W. Mullin, *Crystallization*, Elsevier, 2001.

62 G. G. Libowitz, in *The Chemical Structure of Solids*, Springer, 2012, pp. 335–385.

63 J. Chung, I. Granja, M. G. Taylor, G. Mpourmpakis, J. R. Asplin and J. D. Rimer, *Nature*, 2016, **536**, 446–450.

64 Y. Inada, A. M. Mohammed, H. H. Loeffler and B. M. Rode, *J. Phys. Chem. A*, 2002, **106**, 6783–6791.

65 P. D'Angelo, O. M. Roscioni, G. Chillemi, S. Della Longa and M. Benfatto, *J. Am. Chem. Soc.*, 2006, **128**, 1853–1858.

66 A. A. Dezfoli, M. Mehrabian and H. Hashemipour, *Chem. Eng. Commun.*, 2015, **202**, 1685–1692.

67 A. K. Katz, J. P. Glusker, S. A. Beebe and C. W. Bock, *J. Am. Chem. Soc.*, 1996, **118**, 5752–5763.

68 A. Jakubowska, *J. Chem. Eng. Data*, 2010, **55**, 1876–1881.